Water weakening and the compressive brittle strength of carbonates: Influence of fracture toughness and static friction

Corentin Noël [a,b,*], Barnaby Fryer [a,b], Patrick Baud [c], Marie Violay [b]

[a] *Université Côte D'Azur, CNRS, Observatoire de La Côte D'Azur, IRD, Géoazur, 250 Rue Albert Einstein, 06560, Valbonne, France*
[b] *Laboratory of Experimental Rock Mechanics, Ecole Polytechnique Fédérale de Lausanne, Lausanne, Switzerland*
[c] *Université de Strasbourg, CNRS, Institut Terre et Environnement de Strasbourg, UMR 7063, 5 Rue René Descartes, Strasbourg F, 67084, France*

ARTICLE INFO

ABSTRACT

Water is ubiquitous within the pore space of rocks and has been shown to affect their physical and mechanical behaviour. Indeed, water can act on the rock strength via mechanical (i.e., reducing the effective stresses) or chemical effects (e.g., mineral dissolution, mineral alteration, subcritical crack growth, etc.). As rock macroscopic strength is controlled by both fracture toughness and friction at the grain-scale, these parameters should also be affected in presence of water. While some recent studies have measured the effect of water on both fracture toughness and frictional parameters to constrain the water weakening of porous rock compressive strength, the physical parameters, or rock characteristics, that influence this weakening are as of yet unclear. Here, we report a series of laboratory experiments in order to determine the influence of a water-saturated, as opposed to dry, environment on five limestones' strengths. The uniaxial compressive strength, the mode-I fracture toughness and the static friction parameters are of interest. The experiments show that, for the tested limestones, water-saturated conditions provoke a reduction of the uniaxial compressive strength by up to 53 %. This reduction is accompanied by a reduction of the mode-I fracture toughness by up to 34 % and of the static friction by up to 16 %. Even though the water weakening of the uniaxial compressive strength is not influenced by the sample porosity, the mode-I fracture toughness reduction in the presence of water is accentuated for high-porosity limestones. Additionally, low porosity limestones appear to promote higher static friction reductions in water-saturated environments.

1. Introduction

Water is pervasive in rocks and can affect their mechanical behaviour. In the brittle field, water affects rock strength via both mechanical and chemical effects. The pressurized pore fluid diminishes in-situ effective stresses and brings the rock mass closer to failure.[1–4] In addition to this mechanical effect, water has been shown to affect the rock strength through a large number of mechanisms, including chemical effects such as mineral dissolution/alteration,[5] or subcritical crack growth.[6] Quantifying such weakening is straightforward since it only involves the comparison of mechanical behaviour for dry and water-saturated samples.

A reduction of the brittle strength in presence of water (i.e., water weakening) has been observed for porous rocks such as sandstones,[7–16] limestones,[17–19] gypsum,[20] chalk[21] or porous volcanic rocks.[22,23] The amplitude of the water weakening is variable from one rock to another,

even for the same rock type. Past studies have shown that the mineral content of the rock, and particularly clay content, impact the efficiency of rock water weakening: the higher the clay content, the more significant the water weakening.[16,24,25] However, porous rock, such as sandstones and limestones presenting a very low clay mineral content, also suffer water weakening.[7,13,26–28]

When subjected to compressive stress, the micromechanical response of porous rock is governed by micro-crack nucleation, growth, and coalescence. The development of micro-cracks is predominantly influenced by the fracture toughness of the undamaged material and the frictional strength of pre-existing cracks.[29–32] Based on micromechanics, Baud et al.[26] provided an interpretation of the water weakening observed in sandstones, attributing it to a simultaneous reduction in both microscopic fracture toughness and frictional strength. This interpretation was recently supported by measurements of these parameters in dry and water saturated conditions.[13] Notably, the diminishment of

---

fracture toughness due to water weakening has been documented in various rocks and has been attributed to factors such as stress corrosion cracking,[33] mineral alteration and dissolution,[12] capillary forces at the crack tip,[22] grain contact lubrication,[8] clay weakening[34] or reduction of the surface energy via adsorption.[26] In addition, the frictional strength of rock surfaces (i.e., discontinuity, joint, or fault) can potentially be reduced by the decrease of adhesion forces at the asperity in presence of water[35] acting as a lubricant,[36] or via a reduction of the asperity strength.[37]

In this study, we experimentally investigate the influence of water on the strength of limestones. Limestone was chosen for its ubiquitous presence and extensive utilization across the globe: about 20 %–25 %, of sedimentary rocks, which themselves blanket over 90 % of the Earth's surface. As a result, limestone is subject to thorough examination in various fields such as mining,[38,39] slope stability,[40–43] and historical monument preservation[44] to ensure engineering site safety. Moreover, limestone exhibits a pronounced sensitivity to water presence, making it prone to dissolution, karst formation, and cavity development, thereby presenting substantial challenges for geotechnical operations. If limestones' mechanical behaviour has been widely studied, no systematic study exists of this material regarding the effect of water-weakening and strength reduction which encompasses uniaxial strength, fracture toughness and frictional strength. Here, we specifically analyse the uniaxial compressive strength, mode-I fracture toughness, and frictional strength, exploring the potential reduction of these properties in the presence of water. Our primary objectives are twofold: 1) to determine if the reduction in uniaxial compression strength under water-saturated conditions is proportional to the reductions in fracture toughness and frictional strength, and 2) to identify any physical characteristics (such as porosity or grain size) that may influence the water weakening of limestones.

2. Material and methods

2.1. Starting material

Five limestones were selected for this study: Tavel limestone (North-West of Avignon, France), Indiana limestone (south central Indiana, USA), Saint Maximin limestone (North of Paris, France), Leitha limestone (South-East of Vienna, Austria) and Solnhofen limestone (South Bavaria, Germany). These limestones were selected because they span a large range in porosity for a similar mineral composition. Also, these rocks' mechanical properties are well documented in the literature (for Tavel,[28,45–48] Indiana,[48–58] Saint Maximin limestone,[48,59,60] Leitha,[58,61–63] and Solnhofen[18,64–69]) facilitating comparison and extrapolation of the acquired data.

X-ray diffraction and optical microscope surveys have been performed to characterize these limestones (Table 1 and Fig. 1). The tested limestones are almost pure calcite (≥95 %), with a small fraction of quartz (≤3 %). For Saint Maximin limestone, a small fraction of aragonite (3.5 %) was also found. The average grain size was found to be 5–40, 5–300, 100–200, 5–350, ≤5 μm for Tavel, Indiana, Saint Maximin,

Leitha and Solnhofen limestones, respectively. In the limestone classification of Folk,[70] Indiana, Saint Maximin and Leitha are allochemical limestones, mainly composed of large grains (ooid, pellets, shells clasts, etc.) cemented by a thin grain matrix (micrite). Tavel and Solnhofen limestones are micrites composed only of very small grains.

Before subjecting the samples to deformation, the porosity and density were determined using the triple weight method, which involves weighing the sample in its dry, saturated, and saturated-and-immersed states.[71] The limestones exhibit porosities ranging from 5 % to 41 % and dry bulk densities ranging from 1600 to 2570 g/cm^3 (Table 1). Furthermore, ultrasonic P- and S-wave velocities (V_p and V_s) were measured at a frequency of 1 MHz under both dry and water-saturated conditions (Table 1). Using the measured density (ρ), V_p, and V_s, the dynamic elastic moduli of the samples were calculated in accordance with the ASTM Standard[72]:

$$E = \frac{\left[\rho V_s^2 \left(3V_p^2 - 4V_s^2\right)\right]}{\left(V_p^2 - V_s^2\right)} \tag{1}$$

$$G = \rho V_s^2 \tag{2}$$

$$K = \lambda + \frac{2G}{3} \tag{3}$$

$$\lambda = \rho V_p^2 - 2G \tag{4}$$

$$\nu = \frac{\left(V_p^2 - 2V_s^2\right)}{2\left(V_p^2 - V_s^2\right)} \tag{5}$$

where E, G, K, λ and ν, are the Young, shear, and bulk moduli, Lamé's first parameter and Poisson's ratio, respectively (Table 2).

2.2. Experimental methods and data analysis

Three distinct types of experiments were conducted: uniaxial compression, fracture toughness, and friction experiments. All the experiments were done at EPFL in the Laboratory of Experimental Rock Mechanics. The three different methods used are described in Noël et al.[13]; here only the essential aspects will be mentioned.

To understand the effect of water saturation on the mechanical behaviour of the tested limestones, all experiments were conducted in both dry and water-saturated conditions. For the experiments conducted in a dry environment, the samples were left in a ventilated oven at 105 °C overnight and then placed in a desiccator for at least 5 h. This allows them to cool down without being in contact with room humidity. The deformations were then performed at room temperature. For the experiments conducted in a water-saturated environment, in the following referred to as "saturated", the samples were initially left in a ventilated oven at 105 °C overnight and subsequently saturated under vacuum with deaired distilled water at room temperature. In addition to

Table 1
Mineral composition and physical properties of the five studied limestones. Abbreviations: cal = calcite, qtz = quartz, arg = aragonite.

| Sample	Mineral composition	Average grain size (μm)	Porosity (%)	Bulk dry density (g/cm^3)	Vp (m/s)		Vs (m/s)	
					dry	saturated	dry	saturated
Tavel	96.8 % cal, 3 % qtz	5–40	11.2 ± 0.7	2385 ± 10	4697 ± 83	4749 ± 76	2772 ± 74	2818 ± 44
Indiana	98.5 % cal, 1.4 % qtz	5–300	19.9 ± 0.3	2167 ± 9	4067 ± 145	4214 ± 128	2507 ± 52	2597 ± 236
Saint Maximin	94.9 % cal, 3.5 % arg, 1.5 % qtz	100–200	39.2 ± 1.2	1647 ± 32	2595 ± 206	2742 ± 95	1656 ± 112	1530 ± 174
Leitha	99 % cal, 1 % qtz	5–350	40.7 ± 0.3	1605 ± 8	2502 ± 55	2747 ± 48	1660 ± 38	1493 ± 132
Solnhofen	98.5 % cal, 1.3 % qtz	≤5	4.8 ± 0.8	2568 ± 17	5557 ± 86	5500 ± 137	3255 ± 42	3199 ± 44
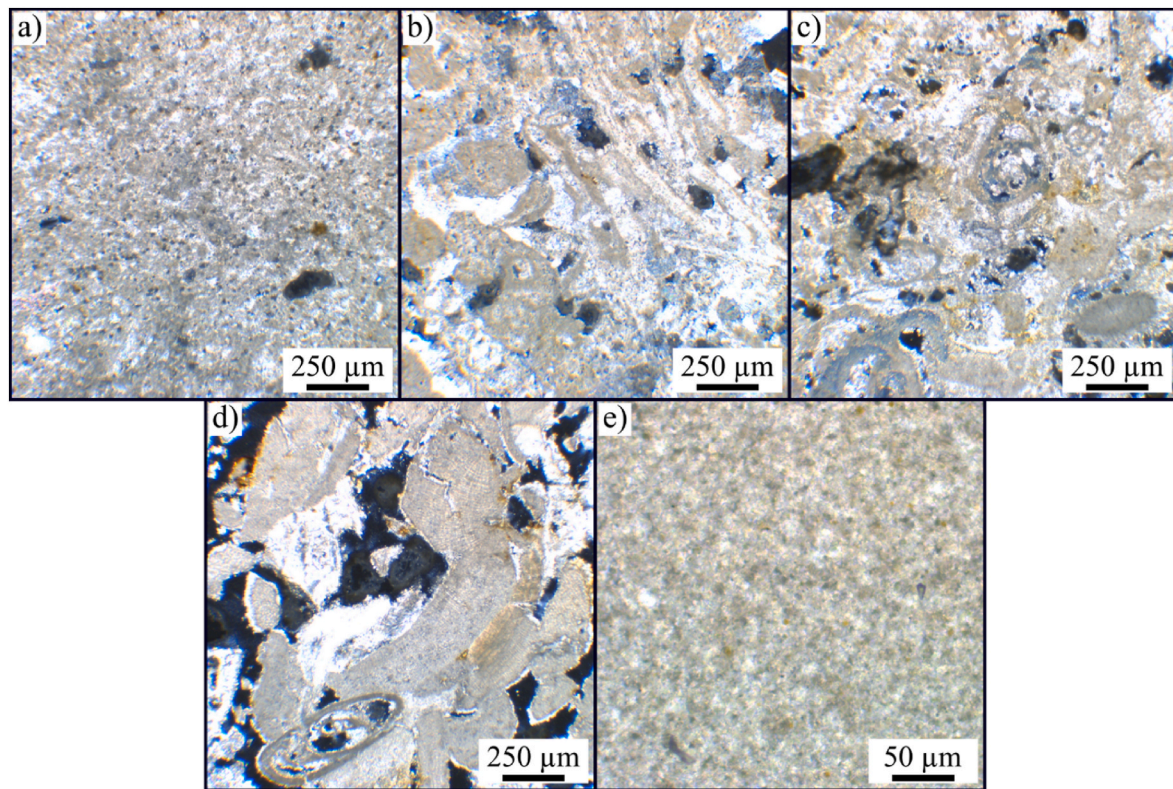
Fig. 1. Optical micrographs taken under cross-polarised light of the tested limestones. a) Tavel, b) Indiana, c) Saint Maximin, d) Leitha and e) Solnhofen.

Table 2
Dynamic elastic parameters measured under dry and water-saturated conditions using the measured density, V_p, and V_s (equations (1)–(5)).

Sample	Dynamic Young's modulus, E (GPa)		Dynamic shear modulus, G (GPa)		Dynamic bulk modulus, K (GPa)		Dynamic Lamé's first parameter modulus, λ (GPa)		Dynamic Poison's ratio, ν	
	dry	saturated	dry	saturated	dry	saturated	dry	saturated	dry	saturated
Tavel	45.2 ± 2.0	46.6 ± 1.5	18.4 ± 1.0	19.0 ± 0.6	28.2 ± 1.5	28.5 ± 1.1	52.7 ± 1.9	53.8 ± 1.8	0.23 ± 0.02	0.23 ± 0.01
Indiana	32.5 ± 1.8	33.8 ± 2.4	13.6 ± 0.6	14.7 ± 2.7	17.7 ± 2.0	18.9 ± 5.6	35.9 ± 2.7	38.6 ± 2.5	0.19 ± 0.02	0.17 ± 0.11
Saint Maximin	10.4 ± 1.8	9.8 ± 2.0	4.5 ± 0.7	3.9 ± 0.9	5.1 ± 1.4	7.2 ± 0.4	11.2 ± 2.0	12.4 ± 1.1	0.15 ± 0.06	0.27 ± 0.05
Leitha	9.8 ± 0.3	9.2 ± 1.1	4.4 ± 0.2	3.6 ± 0.6	4.2 ± 0.5	7.3 ± 1.3	10.1 ± 0.4	12.1 ± 0.5	0.10 ± 0.04	0.28 ± 0.06
Solnhofen	67.4 ± 2.2	65.0 ± 4.0	27.2 ± 0.8	26.3 ± 2.9	43.0 ± 2.0	42.6 ± 4.9	79.3 ± 2.9	77.7 ± 4.2	0.24 ± 0.01	0.24 ± 0.06

the sample being saturated, all experiments conducted under saturated conditions were carried out with the samples immersed in distilled water throughout the deformation process, allowing to maintain saturation levels throughout the deformation (see supplementary material).

2.2.1. Uniaxial compression

For the uniaxial compression experiments, sample cylinders of 36-mm diameter were diamond drilled. For Indiana, Saint Maximin and Leitha limestones, a bedding plane was visible within the rock blocks; therefore, the samples were cored perpendicular to the bedding plane. The opposing faces were then precisely rectified to achieve a final height of 72 mm. The parallelism between the opposing faces was true to within 50 μm.

The uniaxial compression tests were conducted using a hydraulic press from the Walter and Bai company (Figs. S1a and b of the supplementary material and Noël et al.[13]). This equipment allows for the application of an axial stress up to 1 GPa, with a resolution of 50 kPa. During the sample deformation, the axial displacement was measured using two linear optoelectronic transducers mounted close to the sample, with a precision of 1 μm. Radial displacement was measured using an extensometer with a precision of 1 μm mounted on a chain at the centre of the sample. Both the upper and lower pistons used for sample

deformation were fitted with two wideband (200–950 kHz) piezoelectric sensors, enabling the monitoring of Acoustic Emission (AE) events emitted from the samples during deformation. The signals emitted were pre-amplified to 40 dB, and a trigger was established to capture AE events having an amplitude exceeding 0.056 V, approximately 1.75 times higher than the background noise level of the experimental setup.

The deformation of the samples follows the ISRM standards.[73] After positioning the sample between the two pistons, axial deformation was induced by advancing the piston at a velocity of 7.2×10^{-4} mm/s, corresponding to a strain rate of approximately 10^{-5} s^{-1}. The experiments were conducted up to the macroscopic failure of the sample. Throughout the experiments, the recording rate was maintained at 2 Hz. To ensure experimental reproducibility, each uniaxial compression test was performed twice.

The axial displacements recorded were corrected for the elastic deformation of the apparatus, including the press column and pistons. The ratio between the corrected axial displacement and the initial sample length was used to compute the axial strain. Radial strain was determined by comparing the displacement measured at the extensometer to the initial circumference of the sample. The sum of the axial strain and twice the radial strain was used to compute the volumetric strain ($\varepsilon_{vol} = \varepsilon_{ax} + 2\varepsilon_{rad}$).

2.2.2. Mode-I fracture toughness

For the fracture toughness experiments, the Cracked Chevron-notched Brazilian Disk (CCNBD) geometry was employed. This relatively simple geometry allows for stable crack propagation in the specimen. The five limestones were drilled to a diameter of 80 mm. From the obtained cores, disks having a height of 30 mm were sawed and rectified to achieve parallelism within ±100 μm. A notch was then created by inserting 16 mm of a 50.95-mm diameter diamond saw on both sides of the samples at their centre. This preparation is in line with the ISRM suggested methods.[74–77] Note that for Indiana, Saint Maximin and Leitha limestones, as a bedding plane was observed in the blocks, the samples were prepared so that the notch was perpendicular to the bedding.

The fracture toughness experiments were also performed using the Walter and Bai hydraulic press (Figs. S1c and d of the supplementary material and Noël et al.[13]). Here, larger pistons than those used for the uniaxial compression experiments were deployed to simplify the alignment of the samples. In this setup, the system permits an axial force of up to 2 MN with a resolution of 0.5 kN. Throughout sample deformation, axial displacements (parallel to the notch) were monitored using two linear optoelectronic transducers positioned near the sample, with a precision of 1 μm. The measurement of the crack-mouth opening (i.e., the opening of the machined notch) was conducted with a precision of ±1 μm. To do so, an extensometer was fixed using "L-shaped" metal plates glued on each side of the machined notch.

The specimens were positioned between the pistons, aligning the machined notch parallel to the loading force (Figs. S1c and d of the supplementary material). Subsequently, a constant displacement rate of 2.5×10^{-2} mm/s was applied until crack propagation occurred. The choice of this rapid displacement rate was made to ensure that the experiments concluded in less than 10 s (as recommended by the ISRM[76]). Note that low-level cycles of loading, as recommended by the ISRM, were intentionally omitted in this study to prevent low-stress crack propagation, particularly for samples exhibiting low fracture toughness. Throughout the experiments, the recording rate was set to 100 Hz. Each fracture toughness experiment was conducted at least twice to guarantee experimental reproducibility. All experiments were deemed valid, as all the samples failed with a crack propagating parallel to the machined notch (i.e., mode-I fracturing).

The mode-I stress intensity factor (K_I) at the tips of the notch was calculated following the standard methods[74–78] as:

$$K_I = \frac{F_{ax}}{B\sqrt{R}}Y^*, \qquad (6)$$

where F_{ax} is the measured axial force on the sample, B and R are the sample thickness and radius, respectively, and

$$Y^* = u \exp(v\alpha_1). \qquad (7)$$

u and v are constants given by the IRSM norms depending on the sample geometry and α_1 is the ratio between the half-machined crack length and the sample radius. We computed the mode-I fracture toughness, or critical stress intensity factor (K_{Ic}) using equations (6) and (7) for the maximum recorded F_{ax} during the experiments. From the measured K_{Ic} and the dynamic elastic moduli (Table 2), we computed the fracture energy (G_c), assuming plain strain conditions[79]:

$$G_c = \frac{K_{Ic}^2(1 - \nu^2)}{E}. \qquad (8)$$

It's worth noting that the dynamic moduli of each sample were compared to an average of the static moduli measured from uniaxial compression experiments. Importantly, the measured static and dynamic moduli exhibit close similarity (Tables 2 and 3).

2.2.3. Static friction

For the friction experiments, samples were first sawed as rectangular prisms of 70 × 35 × 13 mm and 20 × 35 × 13 mm, and rectified to a

Table 3
Summary of the mechanical data (static Young's modulus, uniaxial compressive strength, fracture toughness) measured under both dry and water-saturated conditions, along with the corresponding water weakening of the measured properties.

Sample	Dry static Young's modulus E_s^{dry} (GPa)	Saturated static Young's modulus E_s^{sat} (GPa)	Dry uniaxial compressive strength UCS^{dry} (MPa)	Saturated uniaxial compressive strength UCS^{sat} (MPa)	Water weakening of compressive strength UCS^{sat}/UCS^{dry}	Dry fracture toughness K_{Ic}^{dry} (MPa.m$^{1/2}$)	Saturated fracture toughness K_{Ic}^{sat} (MPa.m$^{1/2}$)	Water weakening of the fracture toughness $K_{Ic}^{sat}/K_{Ic}^{dry}$	Dry static friction coefficient μ_s^{dry}	Saturated static friction coefficient μ_s^{sat}	Water weakening of the static friction coefficient μ_s^{sat}/μ_s^{dry}
Tavel	43.51 ± 0.85	34.61 ± 2.29	191.80 ± 1.70	124.20 ± 0.71	0.65	1.41 ± 0.04	1.25 ± 0.05	0.89	0.771 ± 0.031	0.705 ± 0.031	0.91
Indiana	26.08 ± 0.85	21.59 ± 1.47	71.35 ± 0.07	51.20 ± 5.94	0.72	0.94 ± 0.04	0.76 ± 0.09	0.81	0.743 ± 0.094	0.693 ± 0.033	0.93
Saint Maximin	4.25 ± 0.10	2.42 ± 0.37	9.80 ± 0.45	4.60 ± 0.71	0.47	0.28 ± 0.02	0.18 ± 0.02	0.66	0.663 ± 0.024	0.536 ± 0.187	0.81
Leitha	4.83 ± 0.11	3.07 ± 1.82	9.35 ± 0.07	6.90 ± 0.28	0.74	0.28 ± 0.05	0.23 ± 0.02	0.82	0.611 ± 0.054	0.559 ± 0.084	0.91
Solnhofen	65.54 ± 5.01	55.69 ± 0.51	240.75 ± 4.74	157.65 ± 7.14	0.65	1.21 ± 0.05	1.19 ± 0.04	0.98	0.768 ± 0.040	0.644 ± 0.043	0.84

precision of 10 μm. The sample surfaces were then polished with a Struers resin-bonded diamond grinding disc, MDpiano 80 (equivalent to no. 80 SiC sand paper).

The experiments were performed in a biaxial apparatus called HighSTEPS (full details of the apparatus can be found in Violay et al.[80]). Stainless steel sample holders were used in a single-direct shear setup, with a sample-to-sample interface on one side and a near-frictionless surface (GLYCODUR®, PTFE-based 3-layer material, having a friction <0.02) on the other side (Figs. S1e and f of the supplementary material and Noël et al.[13]). A horizontal piston provides a normal force (up to 180 kN with a precision of ±0.04 kN) on the samples, and a vertical piston provides a shear force (up to 193 kN with a precision of ±0.04 kN). Piston displacements are measured by optical encoders mounted along each piston, with a resolution of 5 nm.

Once the sample setup was mounted and installed in the apparatus, the two pistons are brought into contact with the sample holders and the horizontal load is increased at 1 MPa/min up to a target value of 1 or 5 MPa. Then, the sample was sheared by lowering the vertical piston at 1 μm/s for 2 mm (enough to reach steady-state friction). Following that, the shear stress was removed, and the normal stress was gradually increased at a rate of 1 MPa/min until reaching the second target. The sample was then subjected to shearing for an additional 2 mm. This process was repeated five times to induce shearing at five different normal stress levels. For Tavel, Indiana and Solnhofen limestones, shearing was performed at 5, 10, 15, 20 and 25 MPa normal stress. For Leitha and Saint Maximin limestones, due to their low compression strength, shearing was performed at 1, 2, 3, 4 and 5 MPa normal stress. Throughout the sample's deformation, the recording rate was set at 10 Hz. Note that these methods follow the ISRM suggested method for the determination of frictional strength.[81]

The elastic distortion of the apparatus was taken into account in order to appropriately measure the normal and shear displacements. The normal and shear stresses applied to the discontinuity (or joint) were calculated by dividing the normal force and shear force by the joint apparent contact area: $\sigma_n = F_n/A$ and $\tau = F_s/A$. The shear stress was corrected for the frictional contributions of the piston and the near-frictionless surface. At each normal stress level, the apparent static shear stress (τ_s), that is, the shear stress at the onset of sliding, was determined. A linear regression of the static shear stress – applied normal stress curves was computed to infer the static friction coefficient (μ_s) of the tested samples. Here, we assumed no cohesion, and thus forced the linear regression through the origin (i.e., $\tau_s = \mu_s\sigma_n$).

3. Results

3.1. Uniaxial compression

For the uniaxial compression experiments, all samples, under dry or water-saturated conditions, exhibit identical mechanical behaviour (Fig. 2 and Fig. S2 in the supplementary material). First, the axial stress as a function of the axial strain curve increases non-linearly. This is attributed to the closure of the microcracks oriented perpendicular and sub-perpendicular to the axial stress. Then, the curve shows a quasi-linear behaviour, indicative of the elastic deformation phase of the sample. The static Young's modulus (E_s) was calculated from the slope of this segment of the curve. The elastic deformation ends upon reaching C′, marking the onset of dilatancy. This is characterized by a departure from linearity in the axial stress – axial strain curve and a notable increase in AE events. Subsequently, the slope of the curve decreases until reaching the peak axial stress (i.e., uniaxial compressive strength, UCS). Following the peak stress, a stress drop occurs and the sample macroscopically fails. Post-experiment macroscopic analyses indicate that the final deformations are primarily localized and brittle, manifesting as shear fractures. In the case of Tavel and Solnhofen limestones, the ultimate macroscopic deformation occurred by axial splitting of the sample.
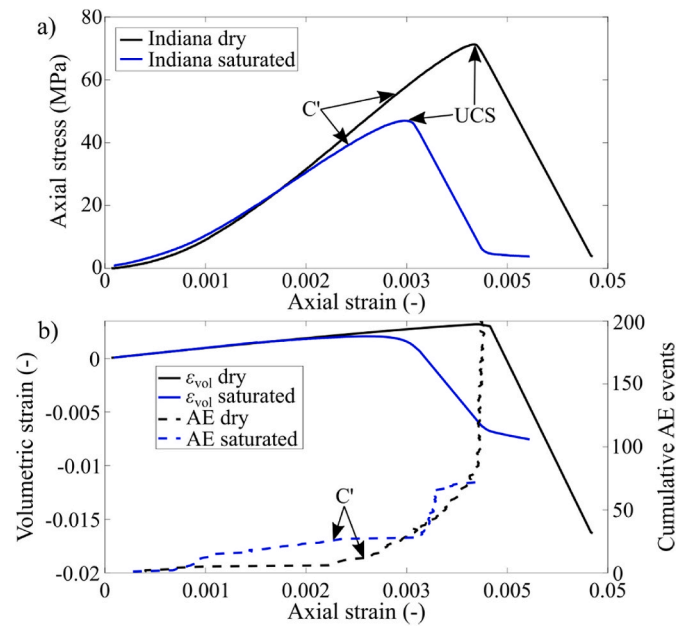

Fig. 2. Characteristic mechanical curves obtained from uniaxial compression experiments, here for Indiana limestone in both dry (black lines) and water-saturated (blue lines) conditions. a) Axial stress plotted against axial strain. b) Volumetric strain and cumulative Acoustic Emission (AE) events as a function of the axial strain. On the curves, we highlight the uniaxial compressive strength (UCS) and the onset of dilatancy (C′). Note that AE events before C′ may originate from the piston-sample frictional interface. The mechanical curves for all tested samples are provided in Fig. S2 of the supplementary material. (For interpretation of the references to colour in this figure legend, the reader is referred to the Web version of this article.)

For all the tested limestones, both the axial stress at C′ and UCS decrease with increasing sample porosity (Fig. 3). Additionally, both the axial stress at C′ and UCS experience a reduction in the presence of water as opposed to dry conditions (Figs. 2 and 3, Table 3 and Fig. S2 in the supplementary material). This reduction depends on the tested limestone: For the axial stress at C', the reduction due to water-saturated conditions is 29, 23, 53, 19 and 29 % for Tavel, Indiana, Saint Maximin, Leitha and Solnhofen limestones, respectively. For the UCS, the reduction is 35, 28, 53, 26 and 35 % for Tavel, Indiana, Saint Maximin, Leitha and Solnhofen limestones, respectively (Table 3). The water-weakening level of these parameters does not depend on the sample porosity (Fig. 4). Note that for all the tested limestones, for water saturated conditions, the total number of AE events are systematically lower than for dry conditions.

3.2. Mode I fracture toughness

For the mode-I fracture toughness experiments, all samples, both under dry and water-saturated conditions, exhibit identical mechanical behaviour (Fig. 5 and Fig. S4 in the supplementary material). First, an elastic behaviour is observed and the mode-I stress intensity factor increases linearly with both the axial displacement and the crack mouth opening. Note that the first part of the K_I – axial displacement curve is not linear and attributed to the sample alignment with the testing apparatus. This phase ends suddenly when the mode-I stress intensity factor reaches a critical (i.e., peak) value, K_{Ic}, after which the sample macroscopically fails. On the K_I – crack mouth opening curve a departure from linearity can be observed slightly prior to reaching K_{Ic}. After K_{Ic}, the stress intensity factor decreases and the crack-mouth opening increases. Post-mortem analyses of the samples revealed that fractures propagated on both sides of the samples from the tips of the notch to the ends of the disc samples. Tavel and Solnhofen limestones also exhibit
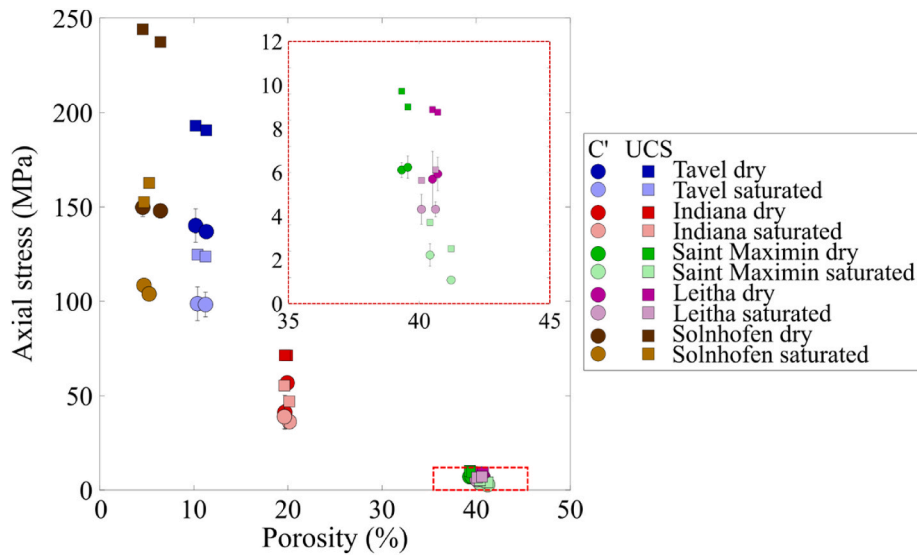
Fig. 3. Axial stresses at the onset of dilatancy (C′, circles) and uniaxial compressive strength (UCS, squares) as a function of porosity for the five tested limestones, both under dry- and water-saturated conditions. For the stress at the onset on dilatancy, the error bars represent the standard deviation between C′ picked using the deviation from linearity in the mechanical data and the onset of AE events. The red rectangle represents a zoom on Saint Maximin and Leitha limestones' data. (For interpretation of the references to colour in this figure legend, the reader is referred to the Web version of this article.)
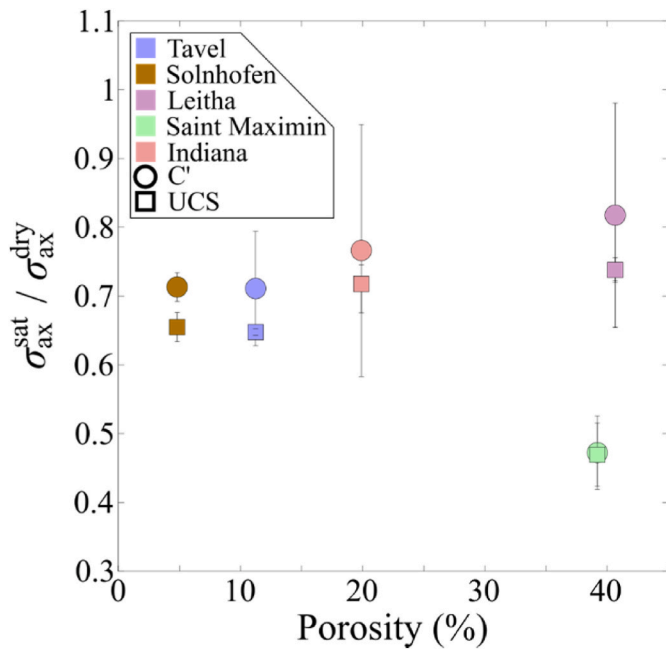

Fig. 4. Ratio between the axial stress under water-saturated conditions, σ_{ax}^{sat}, to the axial stress under dry conditions, σ_{ax}^{dry}, for C′ (circles) and uniaxial compression strength (squares). Each data point represents the average measured water weakening for each limestone tested.

additional cracking sub-parallel to the main aligned-to-notch crack. They were produced after the main aligned-to-notch crack and are due to the fast loading rate imposed during the experiment that kept on pressing the sample after its failure. For the other samples, the formed fractures are aligned with the machined notch so that the experiments are all considered valid (Fig. S5 in the supplementary material).

In general, the fracture toughness (K_{Ic}) decreases with increasing porosity (Fig. 6a). Additionally, for all the tested limestones, the K_{Ic} measured under water-saturated conditions is lower than the one measured under dry conditions (Fig. 6a). The reduction is 11, 19, 34, 18 and 2 % for Tavel, Indiana, Saint Maximin, Leitha and Solnhofen

limestones, respectively. For the tested limestones, the water weakening of K_{Ic} increases with increasing sample porosity (Fig. 7). The fracture energy (G_c) is also influenced by the water saturation. G_c decreases 23, 63, 58 and 35 % in saturated conditions for Tavel, Indiana, Saint Maximin and Leitha limestones, respectively. For Solnhofen limestone, G_c is similar under both dry and water-saturated conditions.

3.3. Static friction

For all friction experiments, the observed frictional behaviour remained consistent for all tested limestones, under both dry and water-saturated conditions (Fig. 8a). At all normal stresses, the shear stress first linearly increases with the shear displacement (i.e., the sample is deforming elastically and the joint is static). Then, the sample reaches its frictional strength and starts to slip (orange circle on Fig. 8a). From this point, the shear stress as a function of the shear displacement decreases and the shear stress rapidly reaches a steady-state. From the picked static shear stresses at each normal stress, the static friction coefficient was computed (μ_s, Fig. 8b–f). Note that if, during the experiments, the sample broke during sliding (Fig. S6 in the supplementary material), the subsequent static shear stresses were not used to compute the static friction coefficient.

The obtained μ_s does not depend on the measured sample porosity (Fig. 9a). However, for all the tested limestones, μ_s measured under water-saturated conditions is lower than under dry conditions, and decreases by 9, 16, 9, 19 and 7 % for Tavel, Indiana, Saint Maximin, Leitha and Solnhofen limestones, respectively (Fig. 8b–f and Fig. 9a). Note that the water weakening is slightly higher for samples with low measured porosity (e.g., Solnhofen Figs. 8f and 9b).

4. Discussion

The conducted experiments emphasize that, for the tested limestones, both UCS and K_{Ic} exhibit a decrease as sample porosity increases, while μ_s remains independent of sample porosity. Furthermore, under water-saturated conditions, UCS experiences a reduction of up to 53 %, K_{Ic} up to 34 %, and μ_s up to 16 %, in comparison to dry conditions (Table 3). Although the reduction in UCS is unaffected by sample porosity, the water weakening of K_{Ic} amplifies with increasing sample porosity. Notably, low sample porosity appears to promote water
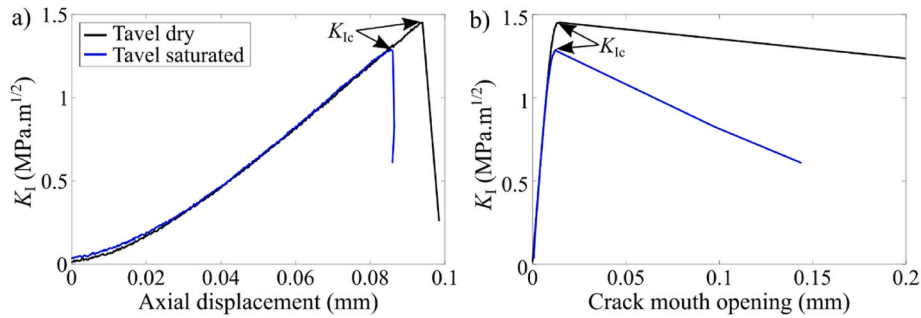
Fig. 5. Characteristic mechanical curves from fracture toughness experiments, here for Tavel limestone under both dry (black lines) and water-saturated (blue lines) conditions. a) Mode-I stress intensity factor as a function of the axial displacement. b) Mode-I stress intensity factor as a function of the crack mouth opening. On the curves, we highlight the mode-I critical stress intensity factor (fracture toughness), K_{Ic}. On these data, the post-peak behaviour should not be considered due to the increase in crack length (i.e., α_1 increases in equation (7), altering the computation of K_I). The mechanical curves for all tested samples are provided in Fig. S4 of the supplementary material. (For interpretation of the references to colour in this figure legend, the reader is referred to the Web version of this article.)
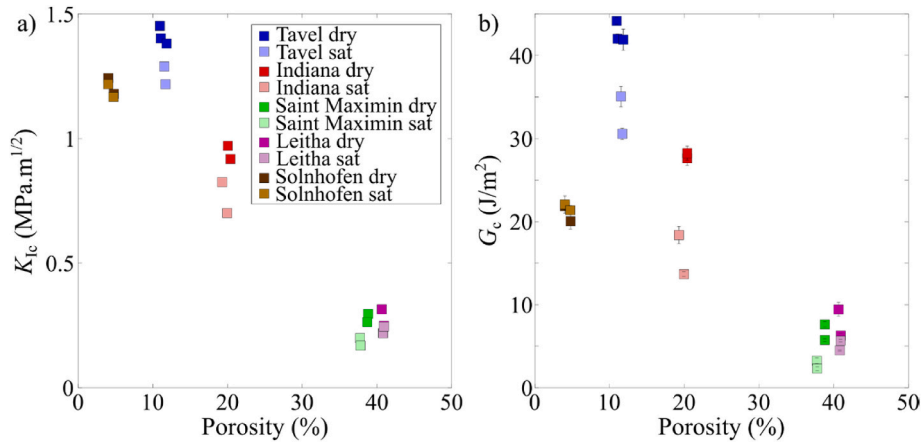
Fig. 6. a) Critical stress intensity factor (or fracture toughness), and b) fracture energy as a function of the sample porosity for the five tested limestones under both dry and water-saturated conditions. The error bars in the fracture energy (G_c) computation show the standard deviation derived from the dynamic elastic moduli calculated from V_p and V_s measurements.

weakening in μ_s.

In the following, we discuss the possible mechanisms involved in the water weakening of limestones. Furthermore, commonly used micromechanical models were tested in order to predict the water weakening of UCS from the measured mode-I fracture toughness and static friction.

4.1. Water weakening of limestones

A reduction of rock mechanical and physical properties has been reported mainly for porous rocks such as sandstones,[7–16,24,82,83] limestones[17–19] or andesite.[22,23] Past studies have shown that the mineral content of the rock, and particularly clay content, impact the efficiency of rock water weakening: the higher the clay content, the larger the water weakening.[16,24,25] However, in the case of the studied limestones, the clay content cannot be responsible for the water weakening as they are all almost 100 % calcite limestones (Table 1).

In the context of compression, whether uniaxial or triaxial, the strength of rock is governed by the initiation, propagation, and merging of micro-cracks.[29–32] In this scenario, the processes of micro-crack nucleation, propagation, and coalescence, collectively known as rock damage, are regulated by micro-scale fracture toughness and static friction. As suggested by Baud et al.,[26] the strength weakening in the presence of water must be caused by a reduction of the fracture toughness (or equivalently fracture energy) and the static friction. Our experiments, as well as previous ones on sandstones,[13] show that the reduction in UCS strength in presence of water is also accompanied by a

reduction of the rock macroscopic fracture toughness and static friction (Figs. 2–9).

For the tested limestones, the very similar initial mineral compositions (Table 1) allow us to remove the effect of mineralogy on water weakening, and focus on effect of porosity.

For K_{Ic}, the water weakening becomes more significant with increasing sample porosity (Fig. 7). While the reduction of the fracture toughness, or fracture energy, with increasing sample porosity has been previously observed for rocks,[84] ceramics[85] or alloys,[86] to the authors' knowledge, the increased water weakening of K_{Ic} with the rock sample porosity has not been observed. For sandstones, Noël et al.,[13] did not see this trend, maybe due to the large mineralogy variation from one sample to another. Under quasi-monomineralic sample conditions, K_{Ic} reduction in the presence of water is often attributed to a reduction of the surface energy at the crack tip due to an adsorption mechanism.[13,26,87] In the present case, such a mechanism, coupled with fast crack propagation may be responsible for the increase of the water weakening of K_{Ic} with increasing sample porosity. Indeed, if the crack propagates faster than the water can diffuse at its tip, the tip of the crack will be saturated if the crack path follows the grain junctions (i.e., in the pre-existing saturated porosity) and dry when propagating within the grains, potentially reducing the water weakening effect for low porosity limestones. Note that the grain size may also affect K_{Ic}[86,88–90] and potentially K_{Ic} water weakening; however, due to the non-homogeneous grain size of the tested limestones, this parameter is difficult to take into account here.

For μ_s, the water weakening is higher for low-porosity samples (Solnhofen limestone) than for the higher porosity ones (Figs. 8 and 9).
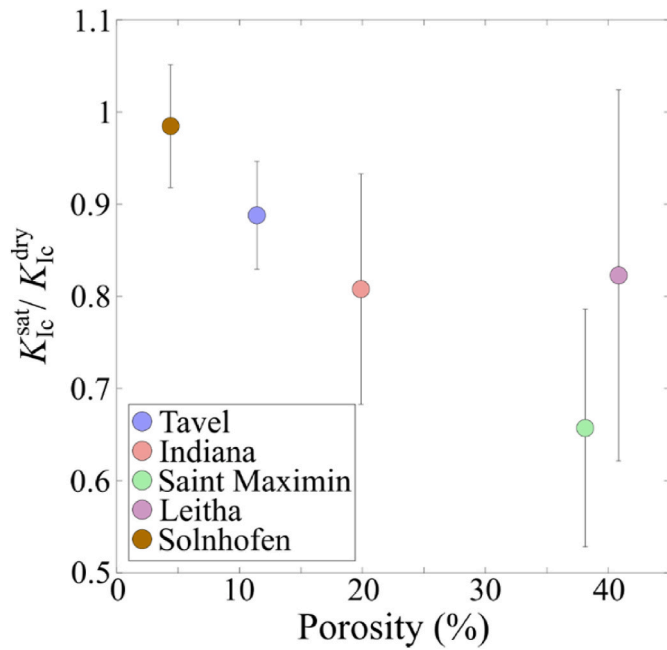
Fig. 7. Ratio between the mode-I fracture toughness measured under water-saturated, $K_{\mathrm{Ic}}^{\mathrm{sat}}$, conditions to the one measured under dry conditions, $K_{\mathrm{Ic}}^{\mathrm{dry}}$. Each data point represents the average measured water weakening for each of the limestones tested.

We propose that the mechanism involved in the water weakening of μ_s is surface lubrication,[36,91] and that the effectiveness of lubrication depends on the surface roughness, i.e., the height and wave length of the asperities. Indeed, for the tested limestones, the initial sample roughness was mainly controlled by the porosity: the higher the porosity, the higher the surface roughness. Therefore, for the low initial porosity (and thus roughness) samples, the water can act as a lubricant on the surface, favouring lower μ_s. However, in cases of high initial sample porosity (and consequently increased roughness), the lubricating effect of water diminishes due to higher imbrication of the two surfaces in contact. Post-mortem analyses of the samples (Fig. S6 in the supplementary material) provide additional support for this explanation. The high-porosity samples generated gouge (i.e., wear material) during shearing in both dry and saturated conditions. In contrast, low-porosity samples only produced gouge under dry conditions and exhibited mirror-polished surfaces under water-saturated conditions.

4.2. Micro-mechanical model ability to predict water weakening in porous rocks

In this section, we evaluate the predictive capacity of two micro-mechanical models (the pore emanating crack model and the wing crack model) to estimate the uniaxial compressive strength (UCS) of the tested limestones using both K_{Ic} and μ_s measurements obtained under dry and water-saturated conditions. A detailed explanation of these micro-mechanical models can be found in Sammis & Ashby[32] for the pore emanating crack model and in Ashby & Sammis[31] for the wing crack model. Moreover, these models have demonstrated reliable predictions for water weakening in sandstones.[13] A concise overview of the two micro-mechanical models is provided here (refer to Baud et al.[92] or Noël et al.,[13] for a comprehensive simplification of the models under water-weakening conditions).

The pore emanating crack model[32] considers an isotropic elastic medium having a given porosity made of homogeneously-distributed spherical pores having the same diameter. With the application of an axial compressive stress on such a medium, a tensile stress concentration, oriented perpendicular to the axial compressive stress, occurs at the

pole of each spherical pore. When the tensile stress concentration reaches the mode-I fracture toughness of the material, cracks nucleate and propagate across the medium. In this model, the length of the cracks emanating from the pores depends on the applied stress on the material. In a crack length – applied stress diagram, the applied stress has a maximum value, being the UCS of the material. Considering the same rock material under different environmental conditions (here dry and water saturated), analytical simplification can be done[92] and the water weakening can be investigated using:

$$\frac{\mathrm{UCS}^{\mathrm{sat}}}{\mathrm{UCS}^{\mathrm{dry}}} = \frac{K_{\mathrm{Ic}}^{\mathrm{sat}}}{K_{\mathrm{Ic}}^{\mathrm{dry}}}. \tag{9}$$

The wing crack model[31] considers an isotropic elastic medium hosting uniformly-distributed penny-shaped cracks oriented at an angle to the axial stress. The application of axial stress induces both shear and normal stresses on each penny-shaped crack. As the axial stress increases, so do the shear and normal stresses. When the shear stress surpasses the frictional strength of the crack (i.e., $\tau \geq \mu_s \sigma_n \ \tau$), sliding occurs, leading to tensile stress at each crack tip. If this tensile stress surpasses the mode-I fracture toughness of the material, wing cracks emanate at the penny-shaped crack tips. The wing crack length – applied stress diagram shows a maximum value in applied stress, being the UCS of the material. Here again, considering the same rock material under dry and water-saturated conditions, an analytical simplification can be done[92] and the water weakening can be investigated using:

$$\frac{\mathrm{UCS}^{\mathrm{sat}}}{\mathrm{UCS}^{\mathrm{dry}}} = \frac{\sigma_{\mathrm{C}}^{\mathrm{sat}}}{\sigma_{\mathrm{C}}^{\mathrm{dry}}} = \frac{K_{\mathrm{Ic}}^{\mathrm{sat}} \Big/ \left(\sqrt{1 + \left(\mu_s^{\mathrm{sat}}\right)^2} - \mu_s^{\mathrm{sat}} \right)}{K_{\mathrm{Ic}}^{\mathrm{dry}} \Big/ \left(\sqrt{1 + \left(\mu_s^{\mathrm{dry}}\right)^2} - \mu_s^{\mathrm{dry}} \right)}, \tag{10}$$

where $\sigma_{\mathrm{C}}^{\mathrm{sat}}$ and $\sigma_{\mathrm{C}}^{\mathrm{dry}}$ are the axial stress at C′ under water-saturated and dry conditions, respectively. Note that the predicted water weakening from the pore emanating crack model depends solely on K_{Ic}, whereas for the wing crack model, both K_{Ic} and μ_s are of importance.

Inserting the macroscopically measured K_{Ic} and μ_s under dry and water-saturated conditions into equations (9) and (10), we can compare the predicted and the measured water weakening of the tested limestones (Fig. 10). The experimentally-measured water weakening of the UCS is globally around 35 % for all the tested limestones (Fig. 4). Fig. 10a and b shows three important features: 1) Based on the measured parameters, both models predict that a major part of the water-weakening could indeed be explained by a reduction of K_{Ic} in the presence of water, except for Solnhofen limestone. 2) The water-weakening predicted by the models is in all cases smaller than the measured weakening under uniaxial compression. 3) Overall, the predictions of wing crack models are slightly closer to the data than the predictions of the pore-crack model, stressing the importance of the changes in μ_s. In detail, there is little difference between the model predictions and the measurements for Indiana and Leitha limestones. These rocks are both allochemical limestones (Fig. 1b and d) but while the pore space in Leitha is dominated by macropores,[61] Indiana limestone has a dual porosity with more than 60 % of its pore space made of micropores of radius <33 μm.[56] This difference does not seem to be important as far as water-weakening is concerned, which could mean that stress-induced damage leading to brittle failure would occur preferentially from the larger pores in these rocks. We also found a decent agreement between the model predictions and the measurements for Saint Maximin limestone, particularly with the wing crack model. Significant scattering in previous mechanical data, due to some heterogeneous porosity distribution in this rock,[60,93] could explain that the results are not as good for this third allochemical limestone. It should also be noted that stress-corrosion cracking has been found to be significant in calcite and limestone[94–97] and could contribute to the observed water-weakening. This contribution is difficult to evaluate, but
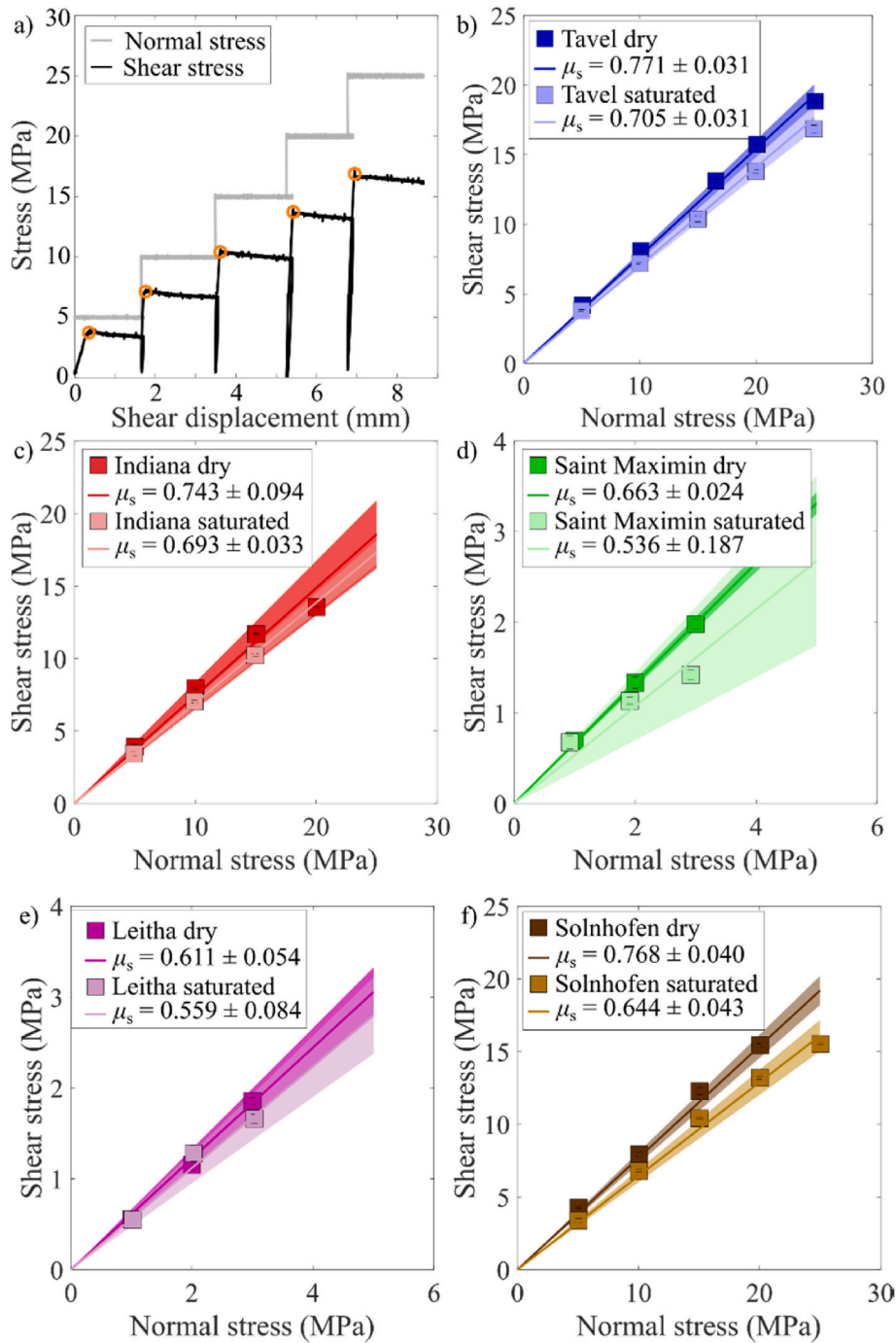
Fig. 8. a) Characteristic mechanical curves from friction experiments, here for Tavel Limestone under water-saturated conditions. Both shear stress (black curve) and normal stress (grey curve) are presented as a function of shear displacement. The orange circles on the shear stress curve represent the picked static friction (μ_s). b-f) Picked μ_s as a function of the applied normal stress under both dry and water-saturated conditions for: b) Tavel, c) Indiana, d) Saint Maximin, e) Leitha and f) Solnhofen limestones. The solid lines represent the best fit of the data and the shaded areas indicate the 95 % confidence interval of the fittings. (For interpretation of the references to colour in this figure legend, the reader is referred to the Web version of this article.)

it would in fact put the model predictions closer to the measurements.

Fig. 10 also shows the poor agreement between both model predictions and our new data on Tavel and Solnhofen, both micritic limestones. In both cases, the predicted water-weakening is less than 10 %, while the measured weakening is about 35 %. Previous studies on Solnhofen limestone[18,67] reported some water-weakening in this rock in agreement with our new UCS data. As for Tavel limetone, Nicolas et al.[28] studied the brittle failure of dry and water-saturated samples up to an effective pressure of 55 MPa. They analysed their data using the wing crack model and concluded that some minor water-weakening is compatible with a reduction of K_{Ic} by <7 % and a larger reduction of μ_s by 42 %. The conclusion of Nicolas et al.[28] appear therefore inconsistent with what is presented here (reduction of 9 % of μ_s in water-saturated conditions). However, our UCS data on both micrites are in line with previous studies. Table 3 shows that the discrepancies between the model results and measurements are mostly due to the fact that K_{Ic} in both rocks was found to change very little in the presence of water. These small variations are not really in agreement with the results of Røyne et al.[94] who reported a 50 % decrease of the surface energy of calcite between dry and wet conditions.
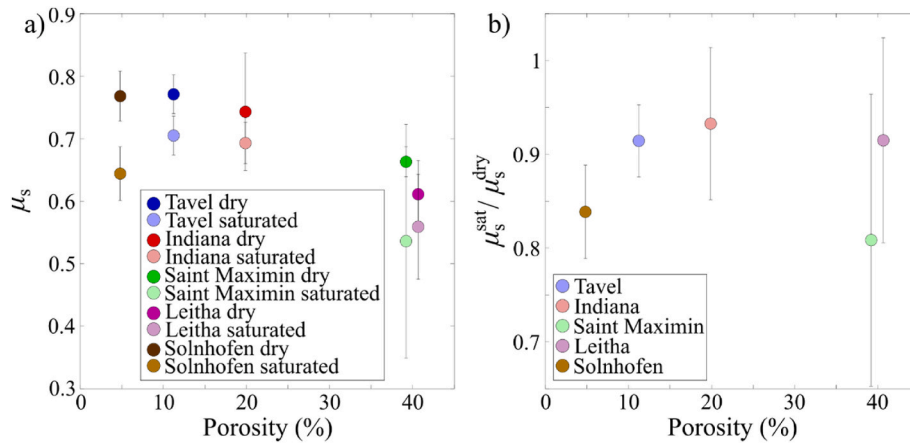
Fig. 9. a) Static friction measured under both dry and water-saturated conditions. b) Ratio between the static friction measured under water-saturated conditions, μ_s^{sat}, to the one measured under dry conditions, μ_s^{dry}. Each data point represents the average measured water weakening for each limestone tested.
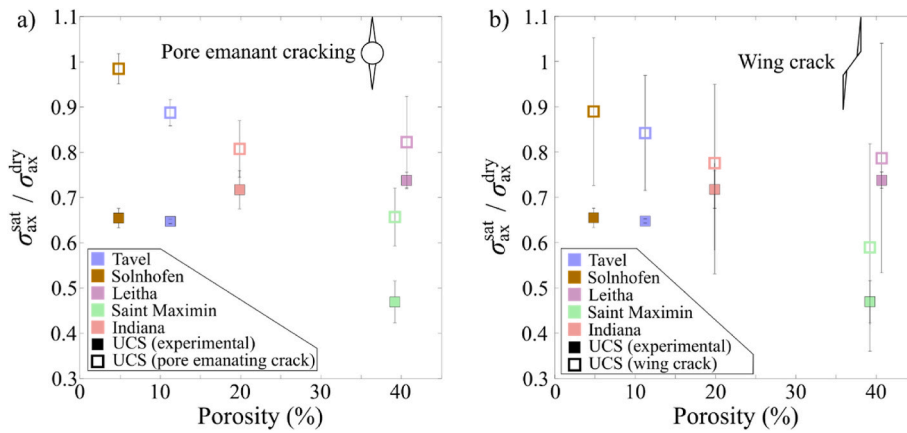
Fig. 10. Ratio of uniaxial compressive strength (UCS) between water-saturated and dry conditions as a function of the sample porosity. Ratios obtained experimentally are shown by the full symbols whereas the data obtained from the micromechanical models are shown with open symbols. a) Pore emanating crack model, and b) wing crack model. The colour corresponds to the limestone tested. Note that water-weakening dependence in the pore emanating crack model is present only in K_{Ic} (equation (9)), while for the wing crack model it is present in both K_{Ic} and μ_s (equation (10)). (For interpretation of the references to colour in this figure legend, the reader is referred to the Web version of this article.)

We noted some differences in the mechanical data used to infer K_{Ic} for Tavel and Solnhofen compared to the other tested limestones. While for Tavel and Solnhofen the K_I vs displacement curves showed an abrupt stress drop occurring as the curve was linear (Fig. 5 and S4 in the supplementary material); failure for the other rocks occurred after a certain amount of plastic strain. Moreover, visual inspection of these samples revealed that the fractures in the micritic limestones were significantly less tortuous than in the more porous end-members (Fig. S5 in the supplementary material). Taken together, these observations suggest that the fractures developed very quickly in the micrites mostly through grains of very small size (typically 5 μm for Solnhofen), in materials of relatively low porosity and low permeability, where water would not diffuse very fast. It is then possible that failure in the K_{Ic} experiments occurred in the micrites in conditions close to dry conditions (i.e., crack propagation faster than water diffusion toward the crack tip). In contrast, the fractures in the other limestones would develop slower, partially or totally along grain boundaries, and in fully drained conditions. The conclusion is then that the K_{Ic} measurements performed in this study on saturated samples using the ISRM standards cannot really be used in the micromechanical models in the case of the micritic limestones. Whether a reduction of K_{Ic} and or μ_s could fully explain the measured weakening in these limestones, even if likely, cannot be demonstrated here. One way forward would be to perform K_{Ic}

measurements under confinement and with some pore fluid pressure. This is beyond the scope of this work but should motivate future studies.

5. Conclusion

After their physical characterisation (porosity, P- and S-wave velocity, dynamic elastic moduli) a set of destructive experiments (uniaxial compression, mode-I fracture toughness and frictional experiments) allowed for the characterisation of five limestones' strengths. Particularly, uniaxial compressive strength (UCS), mode-I fracture toughness (K_{Ic}), and static friction (μ_s) were evaluated. All the experiments were performed both under dry and water-saturated conditions in order to characterize the water weakening of the limestones' strengths. The results show that.

1) For all the tested limestones, UCS (as well as the axial stress at the onset of inelastic strain) and K_{Ic} decrease with increasing sample porosity. However, μ_s does not depend on the sample porosity.
2) For all the tested limestones, UCS, K_{Ic} and μ_s decrease when the experiments are performed under water-saturated conditions. For UCS, water weakening is about 35 % for all tested samples. For K_{Ic}, the water weakening increases from 2 to 34 % when increasing sample porosity from 5 to 40 %. For μ_s, the water weakening is more

pronounced for the two least porous samples compared to the higher porosity ones.

3) Using micro-mechanical models, we infer that the water weakening of the UCS is directly linked to the water weakening of both K_{Ic} and μ_s. However, we under-estimate the water weakening due to the use of macroscopically-measured parameters for grain size mechanisms and due to the intrinsic model simplifications.

The mechanisms involved in the water weakening of K_{Ic} and μ_s remain still unclear. We propose that, under the tested conditions and for the tested limestones: K_{Ic} weakening is due to reduction of the surface energy at the crack tip due to an adsorption mechanism; μ_s weakening is due to lubrication mechanisms in presence of water.

CRediT authorship contribution statement

Declaration of competing interest

The authors declare that they have no known competing financial interests or personal relationships that could have appeared to influence the work reported in this paper.

Data availability

Raw data can be found at https://zenodo.org/records/10598216.

Acknowledgment

Raw data can be found at https://zenodo.org/records/10598216.

Appendix A. Supplementary data

Supplementary data to this article can be found online at https://doi.org/10.1016/j.ijrmms.2024.105736.

References

1. Heard HC. Transition from brittle fracture to ductile flow in Solenhofen limestone as a function of temperature, confining pressure, and interstitial fluid pressure. In: Griggs D, Handin J, eds. *Rock Deformation*. vol. 79. Geological Society of America Memoirs; 1960:193–226.
2. Terzaghi K, Peck RB, Mesri G. *Soil Mechanics In Engineering Practice. 3rd Editio*. John Wiley & Sons; 1996.
3. Handin J, Hager RVJ, Friedman M, Feather JN. Experimental deformation of sedimentary rocks under confining pressure: pore pressure tests. *Am Assoc Pet Geol*. 1963;47(5):717–755.
4. Robinson LHJ. Effect of pore and confining pressures on failure characteristics of sedimentary rocks. *Soc Pet Eng*. 1959;216:26–32.
5. Rutter EH. Pressure solution in nature, theory and experiment. *J Geol Soc London*. 1983;140(5):725–740. https://doi.org/10.1144/gsjgs.140.5.0725.
6. Atkinson BK. Subcritical crack growth in geological materials. *J Geophys Res*. 1984; 89(B6):4077–4114. https://doi.org/10.1029/JB089iB06p04077.
7. Duda M, Renner J. The weakening effect of water on the brittle failure strength of sandstone. *Geophys J Int*. 2013;192(3):1091–1108. https://doi.org/10.1093/gji/ggs090.
8. Guha Roy D, Singh TN, Kodikara J, Das R. Effect of water saturation on the fracture and mechanical properties of sedimentary rocks. *Rock Mech Rock Eng*. 2017;50(10): 2585–2600. https://doi.org/10.1007/s00603-017-1253-8.
9. Hadizadeh J, Law RD. Water-weakening of sandstone and quartzite deformed at various stress and strain rates. *Int J Rock Mech Min Sci Geomech*. 1991;28(5): 431–439. https://doi.org/10.1016/0148-9062(91)90081-V.
10. Heap MJ, Villeneuve M, Kushnir ARL, Farquharson JI, Baud P, Reuschlé T. Rock mass strength and elastic modulus of the Buntsandstein: an important lithostratigraphic unit for geothermal exploitation in the Upper Rhine Graben. *Geothermics*. 2019;77:236–256. https://doi.org/10.1016/j.geothermics.2018.10.003.
11. Liu HD, Liu S, Liu HN, et al. Mechanical deterioration effect and damage evolution characteristics of soft sandstone with different water-immersed heights under uniaxial compression. *Bull Eng Geol Environ*. 2023;82(4). https://doi.org/10.1007/s10064-023-03175-7.
12. Maruvanchery V, Kim E. Effects of water on rock fracture properties: studies of mode I fracture toughness, crack propagation velocity, and consumed energy in calcite-cemented sandstone. *Geomech Eng*. 2019;17(1):57–67. https://doi.org/10.12989/gae.2019.17.1.057.
13. Noël C, Baud P, Violay M. Effect of water on sandstone's fracture toughness and frictional parameters: brittle strength constraints. *Int J Rock Mech Min Sci*. 2021;147, 104916. https://doi.org/10.1016/j.ijrmms.2021.104916.
14. Reviron N, Reuschlé T, Bernard JD. The brittle deformation regime of water-saturated siliceous sandstones. *Geophys J Int*. 2009;178(3):1766–1778. https://doi.org/10.1111/j.1365-246X.2009.04236.x.
15. Zang A, Wagner CF, Dresen G. Acoustic emission, microstructure, and damage model of dry and wet sandstone stressed to failure. *J Geophys Res Solid Earth*. 1996; 101(B8):17507–17521. https://doi.org/10.1029/96JB01189.
16. Zhou Z, Cai X, Ma D, Cao W, Chen L, Zhou J. Effects of water content on fracture and mechanical behavior of sandstone with a low clay mineral content. *Eng Fract Mech*. 2018;193(October 2017):47–65. https://doi.org/10.1016/j.engfracmech.2018.02.028.
17. Vutukuri VS. The effect of liquids on the tensile strength of limestone. *Int J Rock Mech Min Sci Geomech Abstr*. 1974;11(1):27–29. https://doi.org/10.1016/0148-9062(74)92202-5.
18. French ME, Zhu W, Xiao X, Evans B, Prior DJ. Thermally enhanced water weakening of the solnhofen limestone. *J Geophys Res Solid Earth*. 2022;127(3). https://doi.org/10.1029/2021jb022742.
19. Zhu J, Deng J, Chen F, Ma Y, Yao Y. Water-weakening effects on the strength of hard rocks at different loading rates: an experimental study. *Rock Mech Rock Eng*. 2021;54 (8):4347–4353. https://doi.org/10.1007/s00603-021-02482-3.
20. Caselle C, Baud P, Kushnir ARL, Reuschlé T, Bonetto SMR. Influence of water on deformation and failure of gypsum rock. *J Struct Geol*. 2022;163, 104722. https://doi.org/10.1016/j.jsg.2022.104722.
21. Risnes R, Madland MV, Hole M, Kwabiah NK. Water weakening of chalk - mechanical effects of water-glycol mixtures. *J Pet Sci Eng*. 2005;48(1-2):21–36. https://doi.org/10.1016/j.petrol.2005.04.004.
22. Nara Y, Morimoto K, Hiroyoshi N, Yoneda T, Kaneko K, Benson PM. Influence of relative humidity on fracture toughness of rock: implications for subcritical crack growth. *Int J Solid Struct*. 2012;49(18):2471–2481. https://doi.org/10.1016/j.ijsolstr.2012.05.009.
23. Heap MJ, Violay MES. The mechanical behaviour and failure modes of volcanic rocks: a review. *Bull Volcanol*. 2021;83(5). https://doi.org/10.1007/s00445-021-01447-2.
24. Hawkins AB, McConnell BJ. Sensitivity of sandstone strength and deformability to changes in moisture content Sandstones studied. *Q J Eng Geol Hydrogeol*. 1992;25: 115–130. https://doi.org/10.1144/GSL.QJEG.1992.025.02.05.
25. Cai X, Zhou Z, Liu K, Du X, Zang H. Water-weakening effects on the mechanical behavior of different rock types: phenomena and mechanisms. *Appl Sci*. 2019;9(20): 4450. https://doi.org/10.3390/app9204450.
26. Baud P, Zhu W, Wong T fong. Failure mode and weakening effect of water on sandstone. *J Geophisical Res Solid Earth*. 2000;105(B7):16371–16389. https://doi.org/10.1029/2000JB900087.
27. Lisabeth HP, Zhu W. Effect of temperature and pore fluid on the strength of porous limestone. *J Geophys Res Solid Earth*. 2015;120(9):6191–6208. https://doi.org/10.1002/2015JB012152.
28. Nicolas A, Fortin J, Regnet JB, Dimanov A, Gúeguen Y. Brittle and semi-brittle behaviours of a carbonate rock: influence of water and temperature. *Geophys J Int*. 2016;206(1):438–456. https://doi.org/10.1093/gji/ggw154.
29. Brace WF, Paulding BW, Scholz C. Dilatancy in the fracture of crystalline rocks. *J Geophys Res*. 1966;71(16):3939–3953. https://doi.org/10.1029/JZ071i016p03939.
30. Brace WF, Bombolakis EG. A note on brittle crack growth in compression. *J Geophisical Res*. 1963;68(12):3709–3713.
31. Ashby MF, Sammis CG. The damage mechanics of brittle solids in compression. *Pure Appl Geophys*. 1990;133(3):489–521. https://doi.org/10.1007/BF00878002.
32. Sammis CG, Ashby MF. The failure of brittle porous solids under compressive stress states. *Acta Metall*. 1986;34(3):511–526. https://doi.org/10.1016/0001-6160(86)90087-8.

33. Kataoka M, Obara Y, Kuruppu M. Estimation of fracture toughness of anisotropic rocks by semi-circular bend (SCB) tests under water vapor pressure. *Rock Mech Rock Eng*. 2015;48(4):1353–1367. https://doi.org/10.1007/s00603-014-0665-y.

34. Wang JJ, Zhu JG, Chiu CF, Zhang H. Experimental study on fracture toughness and tensile strength of a clay. *Eng Geol*. 2007;94(1-2):65–75. https://doi.org/10.1016/j.enggeo.2007.06.005.

35. Dieterich JH, Conrad G. Effect of humidity on time- and velocity-dependent friction in rocks. *J Geophys Res*. 1984;89(B6):4196–4202. https://doi.org/10.1029/jb089ib06p04196.

36. Cornelio C, Spagnuolo E, Di Toro G, Nielsen S, Violay M. Mechanical behaviour of fluid-lubricated faults. *Nat Commun*. 2019;10(1):1274. https://doi.org/10.1038/s41467-019-09293-9.

37. Jaeger JC. The frictional properties of joints in rock. *Geofis Pura e Appl*. 1959;43(1):148–158. https://doi.org/10.1007/BF01993552.

38. Kodama J, Nishiyama E, Kaneko K. Measurement and interpretation of long-term deformation of a rock slope at the Ikura limestone quarry, Japan. *Int J Rock Mech Min Sci*. 2009;46(1):148–158. https://doi.org/10.1016/j.ijrmms.2008.07.013.

39. Kang SS, Jang BA, Kang CW, Obara Y, Kim JM. Rock stress measurements and the state of stress at an open-pit limestone mine in Japan. *Eng Geol*. 2002;67(1-2):201–217. https://doi.org/10.1016/S0013-7952(02)00155-2.

40. Oztekin B, Topal T, Kolat C. Assessment of degradation and stability of a cut slope in limestone, Ankara-Turkey. *Eng Geol*. 2006;84(1-2):12–30. https://doi.org/10.1016/j.enggeo.2005.11.012.

41. Zerathe S, Lebourg T. Evolution stages of large deep-seated landslides at the front of a subalpine meridional chain (Maritime-Alps, France). *Geomorphology*. 2012;138(1):390–403. https://doi.org/10.1016/j.geomorph.2011.10.006.

42. Korup O. Geomorphometric characteristics of New Zealand landslide dams. *Eng Geol*. 2004;73(1-2):13–35. https://doi.org/10.1016/j.enggeo.2003.11.003.

43. Pánek T, Klimeš J. Temporal behavior of deep-seated gravitational slope deformations: a review. *Earth Sci Rev*. 2016;156:14–38. https://doi.org/10.1016/j.earscirev.2016.02.007.

44. Piau T, Bétard F, Dugast F. Inventory and assessment of geoarchaeosites in the Middle Eure Valley (Paris Basin, France): an integrated approach to geoarchaeological heritage. *Int J Geoheritage Park*. 2023;11(4):669–687. https://doi.org/10.1016/j.ijgeop.2023.05.003.

45. Noël C, Passelègue FX, Violay M. Brittle faulting of ductile rock induced by pore fluid pressure build-up. *J Geophys Res Solid Earth*. 2021;126(3):1–18. https://doi.org/10.1029/2020JB021331.

46. Vajdova V, Zhu W, Natalie Chen T, Wong T fong. Micromechanics of brittle faulting and cataclastic flow in Tavel limestone. *J Struct Geol*. 2010;32(8):1158–1169. https://doi.org/10.1016/j.jsg.2010.07.007.

47. Vincké O, Boutéca MJ, Piau JM, Fourmaintraux D. Study of the effective stress at failure. In: Thimus JF, Abousleiman Y, Cheng AHD, Coussy O, Detournay E, eds. *Poromechanics, A Tribute to Maurice A*. Biot; 1998:635–639.

48. Zhu W, Baud P, Wong T fong. Micromechanics of cataclastic pore collapse in limestone. *J Geophys Res Solid Earth*. 2010;115(B4). https://doi.org/10.1029/2009JB006610.

49. Baud P, Hall S, Heap MJ, Ji Y, Wong T fong. The brittle-ductile transition in porous limestone: failure mode, constitutive modeling of inelastic deformation and strain localization. *J Geophys Res Solid Earth*. 2021;126(5). https://doi.org/10.1029/2020JB021602.

50. Hart DJ, Wang HF. Laboratory measurements of a complete set of poroelastic moduli for Berea sandstone and Indiana limestone. *J Geophisical Res Solid Earth*. 1995;100(B9):17741–17751.

51. Ji Y, Baud P, Vajdova V, Wong TF. Characterization of pore geometry of Indiana limestone in relation to mechanical compaction. *Oil Gas Sci Technol*. 2012;67(5):753–775. https://doi.org/10.2516/ogst/2012051.

52. Meng F, Baud P, Ge H, Wong T fong. The effect of stress on limestone permeability and effective stress behavior of damaged samples. *J Geophys Res Solid Earth*. 2019;124(1):376–399. https://doi.org/10.1029/2018JB016526.

53. Schmidt RA. Fracture-toughness testing of limestone - KIc of Indiana limestone was measured using three-point-bend specimens, and toughness is seen to increase with crack length much like many aluminum alloys. *Exp Mech*. 1976;16(5):161–167. https://doi.org/10.1007/BF02327993.

54. Schmidt RA, Huddle CW. Effect of confining pressure on fracture toughness of Indiana limestone. *Int J Rock Mech Min Sci*. 1977;14(5-6):289–293. https://doi.org/10.1016/0148-9062(77)90740-9.

55. Vajdova V, Baud P, Wong T fong. Compaction, dilatancy, and failure in porous carbonate rocks. *J Geophys Res Solid Earth*. 2004;109(B5). https://doi.org/10.1029/2003JB002508.

56. Vajdova V, Baud P, Wu L, Wong T fong. Micromechanics of inelastic compaction in two allochemical limestones. *J Struct Geol*. 2012;43:100–117. https://doi.org/10.1016/j.jsg.2012.07.006.

57. Walton G, Hedayat A, Kim E, Labrie D. Post-yield strength and dilatancy evolution across the brittle–ductile transition in Indiana limestone. *Rock Mech Rock Eng*. 2017;50(7):1691–1710. https://doi.org/10.1007/s00603-017-1195-1.

58. Wang Y, Meng F, Wang X, Baud P, Wong T fong. Effective stress law for the permeability and deformation of four porous limestones. *J Geophys Res Solid Earth*. 2018;123(6):4707–4729. https://doi.org/10.1029/2018JB015539.

59. Abdallah Y, Sulem J, Bornert M, Ghabezloo S, Stefanou I. Compaction banding in high-porosity carbonate rocks: 1. Experimental observations. *J Geophys Res Solid Earth*. 2021;126(1). https://doi.org/10.1029/2020JB020538.

60. Baud P, Schubnel A, Heap M, Rolland A. Inelastic compaction in high-porosity limestone monitored using acoustic emissions. *J Geophys Res Solid Earth*. 2017;122(12). https://doi.org/10.1002/2017JB014627, 9989-10,008.

61. Baud P, Exner U, Lommatzsch M, Reuschlé T, Wong TF. Mechanical behavior, failure mode, and transport properties in a porous carbonate. *J Geophys Res Solid Earth*. 2017;122(9):7363–7387. https://doi.org/10.1002/2017JB014060.

62. Huang L, Baud P, Cordonnier B, Renard F, Liu L, Wong T fong. Synchrotron X-ray imaging in 4D: multiscale failure and compaction localization in triaxially compressed porous limestone. *Earth Planet Sci Lett*. 2019;528, 115831. https://doi.org/10.1016/j.epsl.2019.115831.

63. Meng F, Huang L, Baud P, Wong T fong. Strain localization in 4D imaged by X-ray computed tomography and digital volume correlation: discrete compaction bands in Leitha limestone. *J Mech Phys Solid*. 2023;171, 105160. https://doi.org/10.1016/j.jmps.2022.105160.

64. Baud P, Schubnel A, Wong T fong. Dilatancy, compaction, and failure mode in Solnhofen limestone. *J Geophys Res Solid Earth*. 2000;105(B8):19289–19303. https://doi.org/10.1029/2000JB900133.

65. Fischer GJ, Paterson MS. Dilatancy during rock deformation at high temperatures and pressures. *J Geophys Res*. 1989;94(B12):17607–17617. https://doi.org/10.1029/JB094iB12p17607.

66. McCormick CA, Rutter EH. An experimental study of the transition from tensile failure to shear failure in Carrara marble and Solnhofen limestone: does "hybrid failure" exist? *Tectonophysics*. 2022;844, 229623. https://doi.org/10.1016/j.tecto.2022.229623.

67. Rutter EH. The effects of strain-rate changes on the strength and ductility of Solenhofen limestone at low temperatures and confining pressures. *Int J Rock Mech Min Sci*. 1972;9(2):183–189. https://doi.org/10.1016/0148-9062(72)90020-4.

68. Rutter EH. The influence of interstitial water on the rheological behaviour of calcite rocks. *Tectonophysics*. 1972;14(1):13–33. https://doi.org/10.1016/0040-1951(72)90003-0.

69. Chandler MR, Meredith PG, Brantut N, Crawford BR. Fracture toughness anisotropy in shale. *J Geophys Res Solid Earth*. 2016;121(3):1706–1729. https://doi.org/10.1002/2015JB012756.

70. Folk RL. Practical petrographic classification of limestones. *Bull Am Assoc Pet Geol*. 1959;43(1):1–38.

71. Guéguen Y, Palciauskas V. *Introduction to the Physics of Rocks*. Princeton University Press; 1994.

72. ASTM Standard D2845-00. ASTM int. Laboratory determination of pulse velocities and ultrasonic elastic constants of rock. *Des D 2845 – 00*; 2000;14(April 1996:1–9. https://www.astm.org/.

73. Bieniawski ZT, Bernede MJ. Suggested methods for determining the uniaxial compressive strength and deformability of rock materials. *Int Soc Rock Mech*. 1979;16(2). https://doi.org/10.1016/0148-9062(79)91451-7.

74. Fowell RJ, Xu C. The cracked chevron notched Brazilian disc test- geometrical considerations for practical rock fracture toughness measurement. *Int J Rock Mech Min Sci Geomech Abstr*. 1993;30(7):821–824. https://doi.org/10.1016/0148-9062(93)90029-D.

75. Fowell RJ, Xu C. The use of the cracked Brazilian disc geometry for rock fracture investigations. *Int J Rock Mech Min Sci Geomech*. 1994;31(6):571–579. https://doi.org/10.1016/0148-9062(94)90001-9.

76. Fowell RJ, Hudson JA, Xu C, Chen JF, Zhao X. Suggested method for determining mode I fracture toughness using Cracked Chevron Notched Brazilian Disc (CCNBD) specimens. *Int J Rock Mech Min Sci Geomech Abstr*. 1995;32(1):57–64. https://doi.org/10.1016/0148-9062(94)00015-U.

77. Fowell RJ, Xu C, Dowd PA. An update on the fracture toughness testing methods related to the cracked Chevron-notched Brazilian disk (CCNBD) specimen. *Pure Appl Geophys*. 2006;163(5-6):1047–1057. https://doi.org/10.1007/s00024-006-0057-7.

78. Xu C, Fowell RJ. Stress intensity factor evaluation for cracked chevron notched brazilian disc specimens. *Int J Rock Mech Min Sci Geomech Abstr*. 1994;31(2):157–162. https://doi.org/10.1016/0148-9062(94)92806-1.

79. Lawn B. *Fracture of Brittle Solids*. Cambridge University Press; 1993, 2nd Editio.

80. Violay M, Giorgetti C, Cornelio C, et al. HighSTEPS: a high strain temperature pressure and speed apparatus to study earthquake mechanics. *Rock Mech Rock Eng*. 2021;54(4):2039–2052. https://doi.org/10.1007/s00603-021-02362-w.

81. Muralha J, Grasselli G, Tatone B, Blümel M, Chryssanthakis P, Yujing J. ISRM suggested method for laboratory determination of the shear strength of rock joints: revised version. *Rock Mech Rock Eng*. 2014;47(1):291–302. https://doi.org/10.1007/s00603-013-0519-z.

82. Pimienta L, Fortin J, Guéguen Y. Investigation of elastic weakening in limestone and sandstone samples from moisture adsorption. *Geophys J Int*. 2014;199(1):335–347. https://doi.org/10.1093/gji/ggu257.

83. Pimienta L, Fortin J, Guéguen Y. Experimental study of Young's modulus dispersion and attenuation in fully saturated sandstones. *Geophysics*. 2015;80(5):L57–L72. https://doi.org/10.1190/geo2014-0532.1.

84. Alber M, Brardt A. Factors influencing fracture toughness KIC from simple screening tests. *Int J Rock Mech Min Sci*. 2003;40(5):779–784. https://doi.org/10.1016/S1365-1609(03)00065-0.

85. Rice RW. Grain size and porosity dependence of ceramic fracture energy and toughness at 22°C. *J Mater Sci*. 1996;31:1969–1983. https://doi.org/10.1007/BF00356616.

86. Simpson LA. Effect of microstructure on measurements of fracture energy of Al2O3. *J Am Ceram Soc*. 1973;56(1):7–11. https://doi.org/10.1111/j.1151-2916.1973.tb12340.x.

87. Atkinson BK, Meredith PG. The theory of subcritical crack growth with applications to minerals and rocks. In: *Fracture Mechanics of Rock*. 1987:111–166.

88. Kumar AS, Kumar BR, Datta GL, Ranganath VR. Effect of microstructure and grain size on the fracture toughness of a micro-alloyed steel. *Mater Sci Eng, A*. 2010;527(4-5):954–960. https://doi.org/10.1016/j.msea.2009.09.027.

89. Gutshall PL, Gross GE. Observations and mechanisms of fracture in polycrystalline alumina. *Eng Fract Mech.* 1969;1(3):463–471. https://doi.org/10.1016/0013-7944(69)90005-8.

90. Tattersall HG, Tappin G. The work of fracture and its measurement in metals, ceramics and other materials. *J Mater Sci.* 1966;1(3):296–301. https://doi.org/10.1007/BF00550177.

91. Cornelio C, Passelègue FX, Spagnuolo E, Toro G Di, Violay M. Effect of fluid viscosity on fault reactivation and coseismic weakening. *J Geophys Res Solid Earth.* 2020;125(1), e2019JB018883. https://doi.org/10.1029/2019JB018883.

92. Baud P, Wong T, Zhu W. Effects of porosity and crack density on the compressive strength of rocks. *Int J Rock Mech Min Sci.* 2014;67:202–211. https://doi.org/10.1016/j.ijrmms.2013.08.031.

93. Baud P, Vinciguerra S, David C, Cavallo A, Walker E, Reuschlé T. Compaction and failure in high porosity carbonates: mechanical data and microstructural observations. *Pure Appl Geophys.* 2009;166:869–898. https://doi.org/10.1007/s00024-009-0493-2.

94. Røyne A, Bisschop J, Dysthe DK. Experimental investigation of surface energy and subcritical crack growth in calcite. *J Geophys Res Solid Earth.* 2011;116(B4). https://doi.org/10.1029/2010JB008033.

95. Brantut N, Heap MJ, Baud P, Meredith PG. Mechanisms of time-dependent deformation in porous limestone. *J Geophys Res Solid Earth.* 2014;119(7):5444–5463. https://doi.org/10.1002/2014JB011186.

96. Nara Y, Kashiwaya K, Nishida Y, Ii T. Influence of surrounding environment on subcritical crack growth in marble. *Tectonophysics.* 2017;706–707:116–128. https://doi.org/10.1016/j.tecto.2017.04.008.

97. Rostom F, Røyne A, Dysthe DK, Renard F. Effect of fluid salinity on subcritical crack propagation in calcite. *Tectonophysics.* 2013;583:68–75. https://doi.org/10.1016/j.tecto.2012.10.023.